

X-ray observations of the galaxy cluster Abell 2029 to the virial radius

S. A. Walker,^{1*} A. C. Fabian,¹ J. S. Sanders¹, M. R. George² and Y. Tawara³

¹*Institute of Astronomy, Madingley Road, Cambridge CB3 0HA*

²*Department of Astronomy, University of California, Berkeley, CA 94720, USA*

³*Department of Physics, Nagoya University, Nagoya, 338-8570, Japan*

ABSTRACT

We present *Suzaku* observations of the galaxy cluster Abell 2029, which exploit *Suzaku*'s low particle background to probe the ICM at radii beyond that which is possible with previous observations, and with better azimuthal coverage. We find significant anisotropies in the temperature and entropy profiles, with a region of lower temperature and entropy occurring to the south east, possibly the result of accretion activity in this direction. Away from this cold feature, the thermodynamic properties are consistent with an entropy profile which rises, but less steeply than the predictions of purely gravitational hierarchical structure formation. Excess emission in the northern direction can be explained due to the overlap of the emission from the outskirts of Abell 2029 and nearby Abell 2033 (which is at slightly higher redshift). These observations suggest that the assumptions of spherical symmetry and hydrostatic equilibrium break down in the outskirts of galaxy clusters, which poses challenges for modelling cluster masses at large radii and presents opportunities for studying the formation and accretion history of clusters.

Key words: galaxies: clusters: individual: Abell 2029 – X-rays: galaxies: clusters – galaxies: clusters: general

1 INTRODUCTION

Suzaku's ability to probe the intracluster medium (ICM) to the virial radius has been shown for a number of relaxed clusters so far (George et al. 2009; Reiprich et al. 2009; Bautz et al. 2009; Hoshino et al. 2010; Kawaharada et al. 2010; Simionescu et al. 2011). The study of the outskirts of galaxy clusters has been prevented until recently due to its low surface brightness, and due to the high levels of background radiation to which X-ray telescopes are exposed. The virial radius broadly represents the boundary between the central cluster which is in hydrostatic equilibrium, and the outskirts where matter is still accreting onto the cluster as it continues to form. These measurements are therefore crucial in understanding the formation history of galaxy clusters, and in constraining models which describe the formation process. They also allow mass estimates of galaxy clusters to be improved by allowing the dynamic state of the ICM to be understood to greater radii, whereas previous mass determinations have extrapolated measurements of the centres of clusters. This increases the accuracy with which galaxy clusters can be used as probes of cosmological parameters (such as in Allen et al. 2008, and Vikhlinin et al. 2009).

Here we add Abell 2029 to the growing collection of clusters which have been investigated to the virial radius.

Abell 2029 ($z=0.0767$) is a relaxed galaxy cluster which has been studied extensively in X-rays with *ASCA* and *ROSAT* (Sarazin et al. 1998, hereafter S98), *BeppoSAX* (Molendi & De Grandi 1999), *Chandra* (Lewis et al. 2002; Clarke et al. 2004; Vikhlinin et al. 2005, 2006), and *XMM-Newton* (Snowden et al. 2008; Bourdin & Mazzotta 2008). It has a large cD galaxy (Uson et al. 1991) whose major axis is aligned in the NE to SW direction, in approximately the same direction as that joining it to nearby Abell 2033.

Along with Abell 2033, Abell 2028 and Abell 2066, Abell 2029 forms a small supercluster (catalogue number 154, Einasto et al. 2001), the closest cluster of which is Abell 2033 at 35 arcmin to the North, as shown in Fig. 1. Abell 2029 provides an excellent opportunity to study how the outskirts of a galaxy cluster are affected by its surroundings. Gastaldello et al. (2010) has suggested that a further cluster, 1RXS J150935.9+084605, is associated with the supercluster, and their locations are shown on Fig. 2.

* Email: swalker@ast.cam.ac.uk

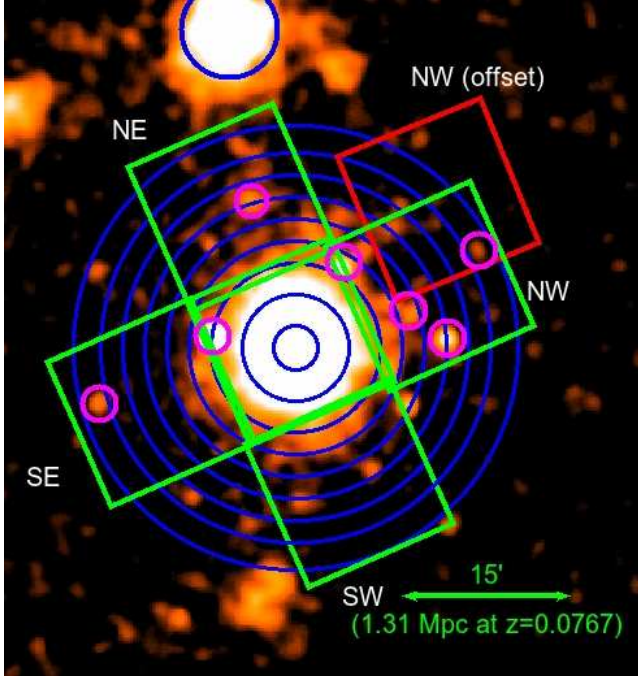


Figure 1. *Suzaku* pointings of A2029 overlaid on a *ROSAT* PSPC image of Abell 2029. The five pointings are in green, the 6th pointing from the public archive is in red. Abell 2033 is highlighted by the blue circle to the North. The blue annuli shown are used in extracting spectra and have ring radii at 2.5', 6.0', 9.5', 12.0', 14.5', 17.0', 19.5', 22.0' and 25.0'. Pointing identifiers are the same as those in Table 1. Extracted point sources are shown circled in pink.

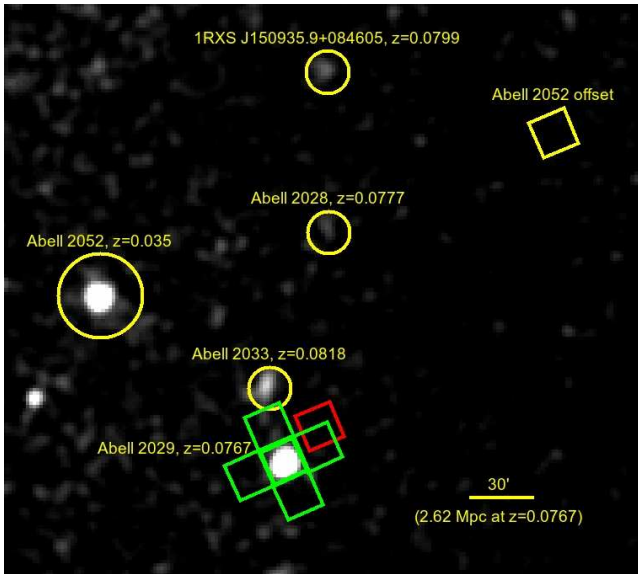


Figure 2. Locations of galaxy clusters in the galaxy supercluster number 154 in the catalogue of Einasto et al. (2001), shown on RASS hard band data. The pointings for Abell 2029 are shown at the bottom of the image. Abell 2066 is omitted as it lies 6 degrees to the South East of Abell 2029. Abell 2052 is at a different redshift and so not associated with the other clusters.

2 OBSERVATIONS AND DATA REDUCTION

Five pointings in a cross formation were obtained during observations with *Suzaku* between 2010 January 28 and 30. A further pointing from the public archive in the north west direction was taken on 2008 January 8 and was also used. An overlay of these pointings is shown in Fig. 1, along with the annuli used in the data analysis. The annular regions used lie between rings at radii 2.5', 6.0', 9.5', 12.0', 14.5', 17.0', 19.5', 22.0' and 25.0'. The low exposure time of the central pointing is compensated by the high surface brightness.

We use HEASoft version 6.11.1, and the calibration database (CALDB) released on 2011 November 10. The raw unfiltered XIS data were cleaned using the AEPIPELINE tool which performs the standard screening described in Tables 6.1 and 6.2 of the *Suzaku* ABC guide¹, and in addition to the default screening criteria we use $COR > 6$ GeV to restrict the geomagnetic cut off rigidity of the particle background, as is typically done (Bautz et al. 2009; Kawaharada et al. 2010). Calibration regions and bad columns were then removed. The defective region in the XIS0 data (defective due to a micrometeorite hit) was excluded. The observations were checked to ensure they weren't contaminated by solar wind charge exchange (SWCX) as described in section 3.5, and the light curves of the observations were checked to ensure that no flaring had occurred. Following the application of all of this filtering, the good exposure times for each pointing are shown in Table 1.

Ancillary response functions (ARFs) and redistribution matrix files (RMFs) are needed to model the response. These were created using the XISSIMARFGEN (Ishisaki et al. 2007) and XISRMFGEN ftools, respectively. The emission we detect can be divided into two broad components; the cluster emission which varies with position on the sky, and the background which is assumed constant on the sky. Since the spatial variation is different for these two components, their responses will be different. We model the response for the background by assuming a uniform background circular region of radius 20' [beyond the size of the XIS field of view (FOV)]. For the cluster emission we use as input to XISSIMARFGEN a model of the surface brightness profile of the cluster. The model we use is the beta model from S98 (their equation 5) obtained using *ROSAT* data in the 0.5–2.0 keV band out to 17', though we note that this fit is not appropriate in the central region ($r < 164''$) due to possible cooling flow regions, and that here the surface brightness is higher than the model predicts. This model has also been found to be consistent with *ASCA* data in both the 0.7–1.5 keV and 3–10 keV bands (Miyoshi et al. 2005), and we show later in section 6 that it is consistent with our *Suzaku* data. For the central region ($r < 164''$) we use the beta model found in Lewis et al. (2002) using *Chandra* data for the surface brightness model, and match the two beta models at $r = 164''$.

It has been found previously (George et al. 2009) that the results are relatively unaffected by changing the surface brightness distribution input to XISSIMARFGEN, so we do not expect possible deviations from the β model in the outskirts to affect the results significantly. Indeed, when the analysis was performed using only the S98 β model as the surface brightness input to XISSIMARFGEN, (which underestimates the surface brightness of the core) the results of the spectral fits were essentially unchanged.

We use only data from the front illuminated (FI) detectors XIS0 and XIS3 owing to the higher background level of the back illuminated (BI) detector XIS1 (George et al. 2009). We use both the

¹ <http://heasarc.gsfc.nasa.gov/docs/suzaku/analysis/abc/>

Table 1. Observational parameters of the pointings

Name	Obs. ID	Position	Total Exposure (ks)	RA	Dec (J2000)
1	804024010	Centre	14.2	227.7409	5.7498
2	804024020	NE	43.4	227.8527	6.0108
3	804024030	SW	33.4	227.6311	5.4874
4	804024040	SE	40.4	228.0053	5.6496
5	804024050	NW	36.0	227.4808	5.8608
6	802060010	NW (offset)	289.2	227.4644	6.0238

3×3 editing mode and the 5×5 editing mode. The spectral fits are performed by fitting the data for each detector and editing mode simultaneously. We use a standard Λ CDM cosmology with $H_0 = 70$ km s $^{-1}$ Mpc $^{-1}$, $\Omega_M = 0.3$, $\Omega_\Lambda = 0.7$. All errors unless otherwise stated are at the 1σ level.

All spectral fits were performed in XSPEC 12.7.0u using the extended C-statistic.

3 BACKGROUND MODELLING AND SUBTRACTION

Accurate measurements of the low surface brightness outskirts of galaxy clusters requires an accurate understanding of the X-ray background and its expected level of variation. The X-ray background can be separated into two main distinct components. One is the cosmic X-ray background (CXB) which consists of unresolved point sources of extragalactic origin, mostly believed to be AGN, and which dominates the background in the 2-10 keV band. The second is soft foreground emission from within our galaxy which is the dominant contributor to the X-ray background at energies below 2 keV; this is the result of hot gas within our galaxy and so the nature of this background component is strongly dependent on the direction of observation. We treat each of these background components separately as follows.

3.1 The CXB

The CXB has been studied extensively by most major X-ray satellites, however measurements of its average flux in the 2-10 keV band have varied between different observatories, as shown in Fig. 10 of De Luca & Molendi (2004). We take the total CXB flux in the 2-10 keV band to be the value from Moretti et al. (2009) using *Swift* data, $2.18 \pm 0.13 \times 10^{-11}$ erg cm $^{-2}$ s $^{-1}$ deg $^{-2}$, which is highly consistent with the value obtained using *XMM-Newton* ($2.24 \pm 0.16 \times 10^{-11}$ erg cm $^{-2}$ s $^{-1}$ deg $^{-1}$ in De Luca & Molendi 2004). These values are higher than those obtained using ASCA in Kushino et al. (2002) which are used to model the CXB in Hoshino et al. (2010) and Akamatsu et al. (2011) in their studies of *Suzaku* data for the outskirts of Abell 1413 and Abell 2142 respectively, which is most likely due to the significant stray light contamination to which the ASCA observations were subjected.

Our *Suzaku* observations allow us to exclude point sources down to a threshold flux of $S_{\text{excl}} = 10^{-13}$ erg cm $^{-2}$ s $^{-1}$ in the 2-10 keV band (and the point sources excluded are shown in Fig. 1). To calculate the unresolved CXB level following the removal of these point sources, we use the source flux distribution found in Moretti et al. (2003) (obtained by fitting to a catalogue of point sources extending down to a flux of 2×10^{-16} erg cm $^{-2}$ s $^{-1}$) to calculate the flux contribution of the resolved sources. We do this instead of integrating the source flux distribution from 0 to the

threshold flux because the source flux distribution is uncertain below the minimum flux studied in Moretti et al. (2003), and indeed when integrated over all energies leads to an underestimate of the total CXB level (see Fig. 5 of Moretti et al. 2003).

The unresolved CXB level (in ergs cm $^{-2}$ s $^{-1}$ deg $^{-2}$) is therefore given by:

$$F_{\text{CXB}} = 2.18 \pm 0.13 \times 10^{-11} - \int_{S_{\text{excl}}}^{S_{\text{max}}} \left(\frac{dN}{dS} \right) \times S dS \quad (1)$$

which, using the two powerlaw best fit for $N(S)$ given in Moretti et al. (2003) gives an unresolved 2-10 keV flux of $1.87 \pm 0.13 \times 10^{-11}$ erg cm $^{-2}$ s $^{-1}$ deg $^{-2}$.

The expected fluctuations in the CXB for a given solid angle, Ω , due to variations in the number of unresolved point sources below the threshold flux in the area of observation can be calculated using (Bautz et al. 2009):

$$\sigma_{\text{CXB}}^2 = (1/\Omega) \int_0^{S_{\text{excl}}} \left(\frac{dN}{dS} \right) \times S^2 dS \quad (2)$$

where we see that the variance decreases with increasing solid angle observed (Ω) and with decreasing threshold flux (S_{excl}).

The expected fluctuations in the CXB for each extraction region examined are shown in table 2. These provide the ranges which must be investigated to understand the effect of the uncertainty of the CXB level on our measurements in the outskirts. These ranges are consistent with those obtained by scaling the fluctuations observed with *Ginga* using the method of Hoshino et al. (2010), and also with the observed variance described in Simionescu et al. (2011) using the *Suzaku* background pointings for the Perseus cluster.

3.2 The soft galactic foreground

Abell 2029 is located well out of the galactic plane, meaning that the absorbing hydrogen column density is low [the mean Leiden Argentine Bonn (LAB) survey (Kalberla et al. 2005) value is 3.26×10^{20} cm $^{-2}$] and that possible variations of the column density across the cluster have a negligible affect on the soft band emission.

Abell 2029 is however located near the North Polar Spur (NPS), which is a region of complex soft band emission attributed to part of a hot interstellar bubble formed from supernova explosions and the outflows of young, hot stars. Previous studies of Abell 2029 and its surrounding region have required extra background components to model the NPS emission, in addition to the background level associated with normal galactic emission. Studies of Abell 2029 with *Chandra* (Vikhlinin et al. 2005) and with *XMM-Newton* (Bourdin & Mazzotta 2008) have used a soft foreground

Table 2. CXB fluctuations in each annulus for each pointing in the 2-10 keV band (10^{-12} erg s $^{-1}$ cm $^{-2}$ deg $^{-2}$)

Position	0.0'-2.5'	2.5'-6.0'	6.0'-9.5'	9.5'-12.0'	12.0'-14.5'	14.5'-17.0'	17.0'-19.5'	19.5'-22.0'	22.0'-25.0'
Centre	6.8	3.1	2.7	-	-	-	-	-	-
NE	-	-	-	6.1	5.0	4.6	4.5	4.5	4.6
SW	-	-	-	5.6	5.0	4.6	4.5	4.6	4.9
SE	-	-	-	5.5	4.6	5.0	4.7	5.2	6.4
NW	-	-	-	6.6	6.5	4.9	5.1	5.3	5.0
NW (offset)	-	-	-	-	-	8.2	5.6	5.7	5.1

model consisting of two unabsorbed MEKAL components, one at 0.46 ± 0.07 keV and the other at 0.22 ± 0.05 keV.

We use the region outside 25' from the north-western offset *Suzaku* pointing to fit for the soft thermal background components, and find that the best fit (shown in Appendix A) is achieved using a model consisting of two unabsorbed APEC components with temperatures at $0.53^{+0.08}_{-0.08}$ keV and $0.20^{+0.05}_{-0.05}$ keV, each of which has its metallicity fixed to $1 Z_{\odot}$. This is consistent with the foreground model used in Vikhlinin et al. (2005) described earlier, which themselves were found to be consistent with previous *Chandra* measurements of the NPS region. To investigate the spatial variation of these background components, we use the ROSAT PSPC pointing of Abell 2029 (observation identifier: rp800249) and extract four background regions (in an annulus between 30' to 50') to the northwest, southwest, northeast and southeast, and fit the spectra in the 0.4-2.0 keV bands after subtracting the particle background as modelled by the ftool PCPARPHA. ROSAT ARFs were created using the ftool PCARF and standard filtering procedures were used as described in the document 'ROSAT data analysis using xselect and ftools'². We find that the spectra are completely consistent with the two APEC component model found using the *Suzaku* region to the north-west, and table 3 shows the spatial variations in the normalisations of the two background components, which we use as a indicator of the extent of expected spatial variations of these soft background components. The fits to the ROSAT data are also shown in Appendix A. These variations will be used later, along with the variations expected in the CXB from table 2, to determine the affect on our fits of our uncertainty in the background model.

When fitting for the soft foreground the CXB is modelled as an absorbed powerlaw of index 1.4 and its normalisation is allowed to be a free parameter. In all cases the CXB normalisation is consistent with the expected level given the level of point source removal.

3.3 Non X-ray Background

We model the non X-ray background (NXB) resulting from interactions with charged particles using the XISNXBGEN ftool, using a database of measurements taken in an interval spanning 150 days before and 150 days after the observations, and subtract this from the spectra.

3.4 Stray light modelling.

Due to broad PSF each annulus contains contributions from neighbouring annuli. In addition, the precollimator is not completely successful in preventing light following undesired paths

(such as back reflection and secondary reflection, as described in Serlemitsos et al. 2007), and so stray light enters each pointing from the bright core.

To understand the magnitude of this effect we use the image of each annulus (taken to be represented by the beta model of S98 which we show later fits our *Suzaku* data well) as input to the ray tracing simulator XISSIM and simulate a 2×10^6 photon exposure for each annulus, and then measure the fraction of photons from each annulus which are spread into the other annuli. The resulting distribution of photons is shown in table 4. We see that the majority of the flux detected in each annulus originated from that annulus, and that in the outskirts the majority of the contamination originates from the nearest innermost annulus which has similar properties to the annulus in question.

We model emission from the central 6.0' (from which the majority of the cluster flux originates) which spreads into the arms of the cross using XISSIM, using the spectra and image of the core as inputs. We model this emission and include it as a background component, and investigate the affect of accounting for this stray light (i.e. the systematic error caused by the stray light) on our fits in section 4.3.

3.5 Solar Wind Charge Exchange

To ensure our observations are not significantly contaminated due to solar wind charge exchange (SWCX) emission we use data from the Solar Wind Ion Composition Spectrometer (SWICS) on the Advanced Composition Explorer (ACE) spacecraft. We follow Snowden et al. (2004), which assumes that the SWCX is negligible when the ratio of O^{7+} to O^{6+} is below ~ 0.2 (this criterion is also used in Humphrey et al. 2011), and we show in figure 3 that only very small time intervals need to be excluded because of this, and that O^{7+}/O^{6+} does not increase substantially above 0.2 during the times of observation.

4 MODELLING CLUSTER EMISSION

We fix the X-ray background model using the CXB level determined in section 3.1 following point source subtraction and model the CXB as an absorbed powerlaw of index 1.4, added to the galactic components (two APEC components) found in section 3.2 by fitting to the outer annuli of the north western offset pointing (which are found to be consistent with ROSAT results for a background annulus between 30'-50' around the cluster). Later we will investigate the systematic error of fixing the background by varying its parameters within the confidence regions we determined in section 3.

² heasarc.gsfc.nasa.gov/docs/rosat/ros_xselect_guide/xselect_ftools.html

Table 3. Soft foreground fluctuations from ROSAT PSPC and *Suzaku* data. The units of the APEC normalisations are $10^{-14}(4\pi)^{-1}D_A^{-2}(1+z)^{-2} \int n_e n_H dV$, where D_A is the angular size distance (cm), and n_e and n_H are the electron and hydrogen densities (cm^{-3}) respectively, and these values are scaled for a circular area of sky of $20'$ radius (1257 arcmin^2).

Position	0.53 keV APEC norm	0.20 keV APEC norm
ROSAT NE	$5.5^{+0.6}_{-0.6} \times 10^{-4}$	$3.0^{+0.1}_{-0.1} \times 10^{-3}$
ROSAT SE	$6.1^{+0.7}_{-0.7} \times 10^{-4}$	$3.6^{+0.2}_{-0.2} \times 10^{-3}$
ROSAT NW	$6.1^{+0.5}_{-0.5} \times 10^{-4}$	$2.9^{+0.1}_{-0.1} \times 10^{-3}$
ROSAT SW	$6.9^{+0.9}_{-0.9} \times 10^{-4}$	$4.3^{+0.3}_{-0.3} \times 10^{-3}$
SUZAKU NW offset (25'-29')	$6.8^{+0.3}_{-0.3} \times 10^{-4}$	$3.5^{+0.3}_{-0.3} \times 10^{-3}$
SUZAKU NW offset (29'-34')	$6.7^{+0.5}_{-0.5} \times 10^{-4}$	$3.4^{+0.3}_{-0.3} \times 10^{-3}$

Table 4. Percentage contribution of flux in the rows' annulus from the columns' annulus due to PSF spreading and stray light.

	0.0'-2.5'	2.5'-6.0'	6.0'-9.5'	9.5'-12.0'	12.0'-14.5'	14.5'-17.0'	17.0'-19.5'	19.5'-22.0'
0.0'-2.5'	95.9	3.9	0.05	0.002	0.0002	0.0004	0.0004	0.0001
2.5'-6.0'	36.2	60.2	3.5	0.04	0.009	0.004	0.003	0.002
6.0'-9.5'	14.5	19.8	64.4	1.1	0.07	0.02	0.02	0.01
9.5'-12.0'	6.7	3.5	15.9	63.7	9.1	0.7	0.2	0.05
12.0'-14.5'	7.6	3.5	4.0	13.8	62.5	7.3	0.8	0.2
14.5'-17.0'	4.3	1.6	2.3	1.9	15.4	62.8	11.1	0.6
17.0'-19.5'	1.3	1.0	1.3	1.1	2.0	19.8	65.8	7.4
19.5'-22.0'	5.2	1.2	1.0	0.7	1.1	3.0	19.8	65.1

4.1 Projected fits

First of all we do projected fits, modelling each annulus as an APEC component absorbed by a column density of $3.26 \times 10^{20} \text{ cm}^{-2}$ (from the LAB survey) using the PHABS absorption model. We fit to 0.7-7.0 keV band and for the central 3 annuli we allow the metallicity to be a free parameter. In the 0.0'-2.5', 2.5'-6.0' and 6.0'-9.5' annuli the best fit projected metallicities are $0.45^{+0.03}_{-0.03} Z_\odot$, $0.3^{+0.08}_{-0.08} Z_\odot$ and $0.2^{+0.1}_{-0.1} Z_\odot$, which are reasonably consistent with the metallicities found in Vikhlinin et al. (2005). In the annuli outside 9.5' the metallicity is fixed to $0.1 Z_\odot$ as it is not constrained in fits (this is the value obtained in Vikhlinin et al. 2005 in the outskirts). We find that varying the metallicity in the outskirts through a reasonable range (from $0 Z_\odot$ to $0.3 Z_\odot$) has a negligible affect on the fitting parameters. We fix the redshift to 0.0767. We tie the temperatures of the outer 3 annuli due to the low number of counts in the outermost annuli, but let their normalisations be free between them.

We initially examined each direction separately and searched for significant azimuthal variations which would make averaging over certain directions inappropriate. We find two main sources of asymmetry: firstly the temperature is lower in the south eastern direction than in the other directions which are consistent with one another. This is shown in Fig. 6 (the deprojected temperatures shown there are consistent within errors with the projected temperatures, which has also been observed in Bautz et al. 2009 and Akamatsu et al. 2011). This lower temperature to the south east coincides with a depression in temperature seen in the temperature map produced using *XMM-Newton* data in Bourdin & Mazzotta 2008 to the south east, suggesting a disturbance of the ICM in this direction extending from the core of the cluster all the way to the outskirts, possibly due to the accretion of small galaxy groups in this direction.

Secondly the projected density is highest to the north and flat-

tens off (see Fig. 4) and this is the only direction in which we detect statistically significant emission beyond 22'. This indicates the presence of excess emission above the azimuthal average which may indicate a filament structure to the north connecting Abell 2029 and Abell 2033, or emission from Abell 2033 entering the field of view. We investigate this in depth in section 6.

4.2 Deprojected fits

We perform two deprojection runs. The first averages over all of the directions except for the northern direction (where excess emission exists, rendering deprojection impossible in this direction), and the south eastern direction (which has a lower projected temperature and entropy than the other directions). In the second the south eastern direction is deprojected individually due to its lower temperature and entropy.

To achieve the deprojection we fit all nine annuli simultaneously, with each annulus modelled as the superposition of the emission from the shell associated with the annulus and the emission projected into that annulus from shells exterior to it under the assumption of spherical symmetry (thus emulating the PROJECT mixing model by adding multiple APEC components as is done in Humphrey et al. 2011, which allows data from multiple *Suzaku* instruments and pointings to be fitted simultaneously). The temperature is tied for the 3 annuli between 17' and 25' and for the 3 annuli between 9.5' and 17' due to the limited spectral quality of the data. The resulting deprojected temperatures are consistent with the projected ones. The deprojected temperature, density and entropy ($S=kT/n_e^{2/3}$) profiles are shown in Fig. 6 for the azimuthal average and the south eastern direction separately.

The lower temperature in the south eastern direction causes the entropy profile to flatten indicating significant deviation from hydrostatic equilibrium. The temperature profile to the

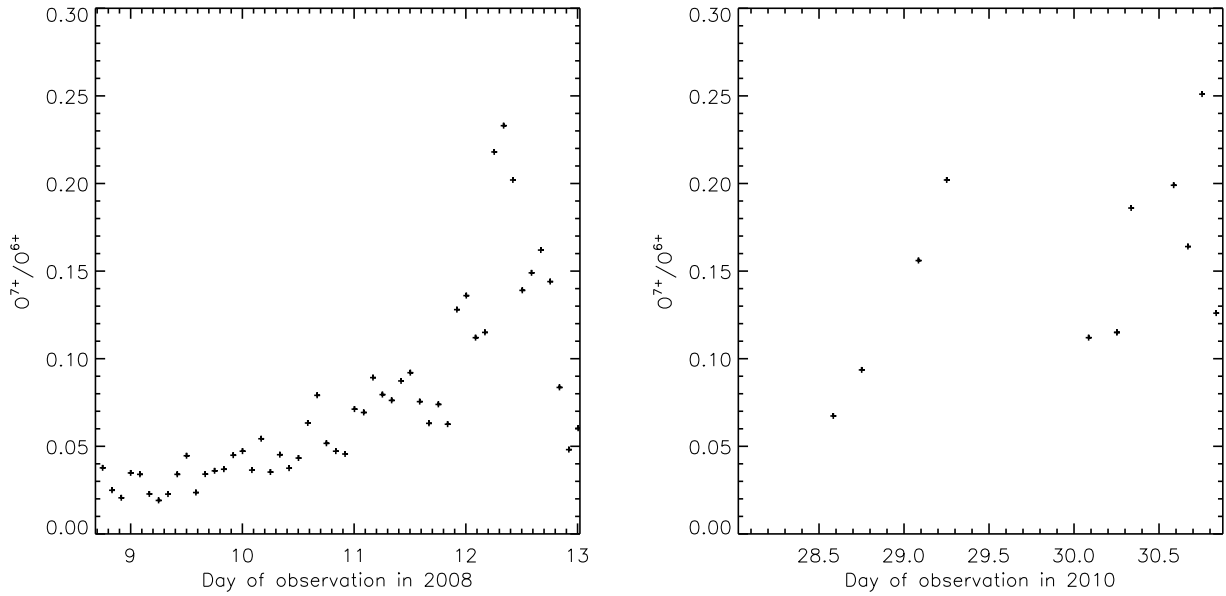


Figure 3. O^{7+}/O^{6+} ratio as measured by the ACE spacecraft. SWCX is assumed to be negligible when O^{7+}/O^{6+} is below ~ 0.2 , and regions above this level are excluded. Left is for the observation taken in 2008 (802060010), and right is for the time region of the observations in 2010 (804024010, 804024020, 804024030, 804024040, 804024050). The day of observation time axis label is the day of the year on which the observation took place.

south east maps on well to the temperature profile found in Bourdin & Mazzotta (2008) for the low temperature region they find to the south east (within 8 arcmins of the core), and is overplotted in blue in Fig. 6. The lower entropy profile from *XMM-Newton* in the central 8 arcmins also maps on well to the flatter and lower entropy we find in the outskirts to the south east, suggesting that the ICM has been disturbed from equilibrium from the outskirts to near the core, possibly due to the accretion of small galaxy groups along this direction (as was suggested in Bourdin & Mazzotta 2008).

Due to *Suzaku*'s large PSF it is not possible to divide the inner two annuli into sectors corresponding to the arms of the cross, but when the 3rd annulus (between $6.0''$ - $9.5''$) is divided we find a statistically significant drop in the temperature below the azimuthal average, which is consistent with the *XMM-Newton* temperature in the same region, as shown in the left column of Fig. 6.

For the azimuthally averaged fits the entropy profile rises with increasing radius, but less steeply than the $r^{1.1}$ relation derived in Voit et al. (2005) assuming purely gravitational hierarchical structure formation (and neglecting non gravitational processes such as feedback, cooling and star formation).

The temperature profile for all directions neglecting the south east is consistent with what has previously been found using *Chandra*, *Swift* and *XMM-Newton*, as shown in Fig. 5 and Fig. 6. The de-projected density profile in all directions is consistent with the extrapolated best fit model to *Chandra* data in (Vikhlinin et al. 2006) when systematic errors in the background modelling are taken into account, as shown in Fig. 6.

4.3 Systematic errors

We need to understand the contribution of the uncertainty of the background model to the error budget. The normalisations of the CXB and the galactic components, (and the temperatures of the galactic components) are only known to an accuracy described in

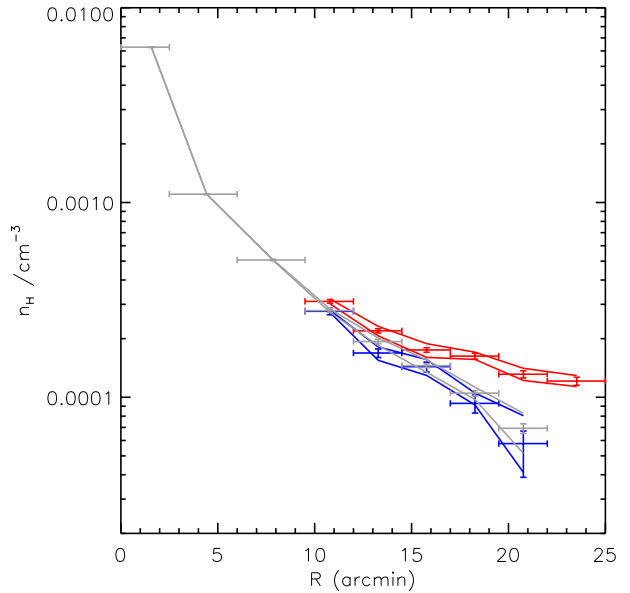


Figure 4. Comparing projected densities. Grey is the azimuthal average excluding the north. Blue is for the low temperature south eastern direction. Red is for the northern direction, showing a significant excess. Solid lines show 1σ systematic errors calculated as described in section 4.3.

section 3, so we need to see the effect on our fits by exploring the possible background parameter space. Typically (for example George et al. 2009 and Akamatsu et al. 2011), these systematic errors have been quantified by varying only one parameter at a time and leaving the others unchanged, which underestimates the actual uncertainty.

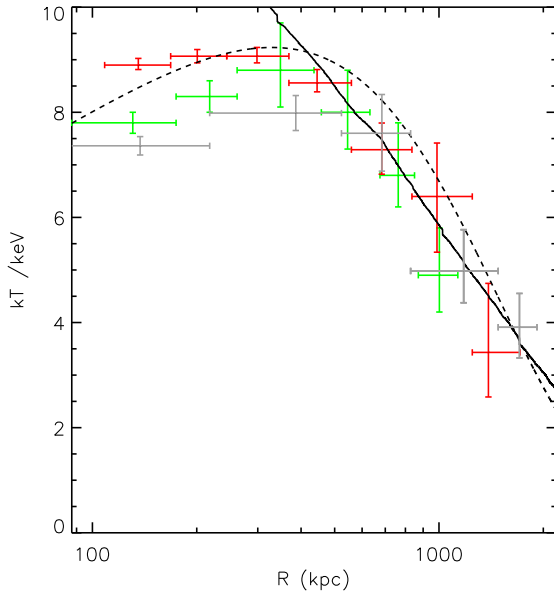


Figure 5. Comparing *Suzaku* temperature profiles with projected temperatures obtained with *Swift* in Moretti et al. (2011) (green) and *Chandra* (red) in Vikhlinin et al. (2006). Grey crosses are azimuthally averaged *Suzaku* temperatures, (excluding the north and the south east). The black dashed line is the deprojected temperature from *Chandra* in Vikhlinin et al. (2006) and the solid black line shows the best fit profile from 6' to 22' to the deprojected *Suzaku* temperatures.

Here we compute the systematic uncertainty of the background model on our deprojected fits by producing 10000 random realisations of the background parameters [the CXB normalisation, the 0.53 and 0.20 keV galactic APEC component normalisations and temperatures, and the NXB level (which has an uncertainty of ± 3.6 percent from Tawa et al. 2008) distributed by their expected variance and performing the deprojected fit for each. In this way the systematic uncertainty in the background is folded into the deprojection to give a complete propagation of the uncertainty in the background to the uncertainty in the spectral fits. The one sigma systematic errors on the temperature, density and entropy profiles resulting from this process are shown for the deprojected fits in Fig. 6. For the temperature the systematic error is roughly of the same order as the statistical error (except in the outermost bin), but for the density it is the dominant source of uncertainty in the outer 4 annuli.

The systematic errors are also calculated for the projected density and shown in Fig. 4, showing that the excess to the north is still statistically significant. Note that because these are projected fits the errors are smaller than for the deprojected fits (because for the deprojected fits the error on the outer annuli is propagated to the error on the inner annuli).

We then perform all the deprojected fits with the stray light level from the central 6' (as simulated by XISSIM) subtracted, and plot as the green line in Fig. 6 the best fit results with this stray light subtracted. In all cases the effect of taking into account the stray light is within the systematic error of the background modelling.

We vary the contamination level on the optical blocking filter (OBF) by ± 10 percent as described in Akamatsu et al. (2011), using the *Suzaku* ftool XISCONTAMICALC to modify the ARFS, and find this to have a negligible effect on the fits.

5 MASS ANALYSIS

Assuming hydrostatic equilibrium and spherical symmetry the total mass interior to radius r is given by (Vikhlinin et al. 2006)

$$M(< r) = -3.68 \times 10^{13} M_{\odot} T(r) r \left(\frac{d \ln n_H}{d \ln r} + \frac{d \ln T}{d \ln r} \right) \quad (3)$$

where T is in keV and r is in Mpc. We find best fit temperature and density profiles by using Monte Carlo methods with 10000 trials, and use these profiles in equation 3 to yield the gravitational mass profile and its 1σ error. The density profile is fit as a beta model of the form $n_H = n_0(1 + (r/r_{cn})^2)^{-\beta}$, and the temperature profile is fit with the function $T = T_0(1 + r/r_{cT})^{\alpha}$ as used in Akamatsu et al. (2011) and Burns et al. (2010). We do this for the azimuthally averaged profiles shown in the left hand column of Fig. 6 (thus excluding the north due to its excess emission and the south east due to its lower temperature and entropy which means that it is likely out of hydrostatic equilibrium). From this we then calculate an estimate of r_{200} (the radius within which the mean density is 200 times the critical density of the universe), which is widely used as an approximation to the virial radius. The cumulative gas mass is calculated using the number density of the ICM derived from the APEC normalisation and assuming spherical symmetry, allowing the gas mass fraction, f_{gas} , as a function of radius to be derived.

The slightly shallower and lower temperature profile we find compared to Vikhlinin et al. (2006), together with the slightly higher density in the outskirts causes our total mass estimate to be lower, and gas mass estimate to be higher, making our measurement of the gas mass fraction in the outskirts higher than those presented in Vikhlinin et al. (2006). This consequently means that our estimate of r_{200} is smaller. We find $M_{500} = 7.2^{+1.1}_{-1.2} \times 10^{14} M_{\odot}$, which is consistent with the Vikhlinin et al. (2006) value of $M_{500} = 8.01 \pm 0.74 \times 10^{14} M_{\odot}$. We find $r_{200} = 1.92^{+0.11}_{-0.13}$ Mpc (corresponding to $22.0^{+1.3}_{-1.4}$ arcmins), with $M_{200} = 8.0^{+1.5}_{-1.5} \times 10^{14} M_{\odot}$, which is smaller than the value obtained using the scaling relation of Arnaud et al. (2005) :

$$\begin{aligned} M_{200}/M_{\odot} &= 5.74 \pm 0.3 \times 10^{14} \left[\frac{kT}{5 \text{ keV}} \right]^{1.49 \pm 0.17} / E(z)^{1/2} \quad (4) \\ E(z) &= [\Omega_m(1+z)^3 + 1 - \Omega_m] \quad (5) \end{aligned}$$

which yields $M_{200} = 12.1^{+0.7}_{-0.8} \times 10^{14} M_{\odot}$ and $r_{200} = 25.3^{+0.6}_{-0.6}$ using the mean spectroscopic temperature of 8.47 ± 0.09 keV from *Chandra* obtained in Vikhlinin et al. (2006). Part of this discrepancy is, as described in Bautz et al. (2009) (which similarly finds a lower mass and r_{200} than derived using *Chandra* results and scaling relations), likely due to the fact that *Chandra* reports temperatures for hot clusters which are systematically higher than those from *XMM-Newton*. This can be seen by comparing the *XMM-Newton* temperature points in Fig. 6 with the *Chandra* points in Fig. 5, and it is believed to be due to the uncertainty in the contamination on the *Chandra* mirrors. Our *Suzaku* results suggest a lower emission averaged spectroscopic temperature of 7.5 ± 0.1 keV (which is consistent with the average temperature of 7.45 ± 0.19 found with ASCA in Fukazawa et al. 2004 and is more consistent with the *XMM-Newton* temperatures), which when used in equation 4, gives $M_{200} = 10.1^{+0.6}_{-0.6} \times 10^{14} M_{\odot}$ and $r_{200} = 23.8^{+0.5}_{-0.5}$ arcmins, which are consistent with the values derived from our *Suzaku* fits.

The gas mass fraction is shown in Fig. 7, which rises with radius and reaches the cosmic mean baryon fraction (0.167, obtained

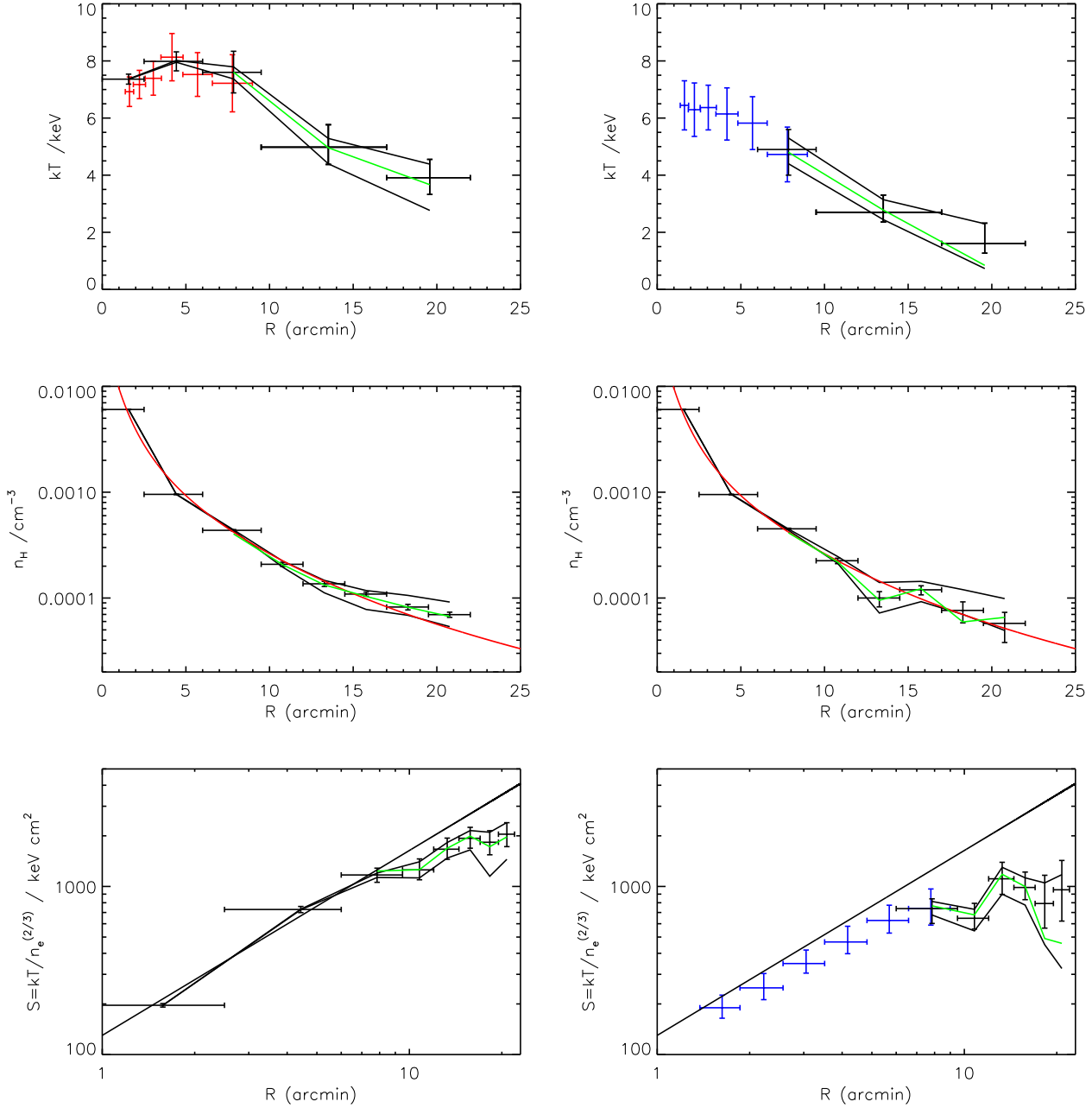


Figure 6. Deprojected temperature, density and entropy profiles. Left column is for the azimuthal average (excluding the north which has excess emission and the south east which has a lower temperature and density). Right column is for the south eastern direction which has a lower outskirts temperature and flatter entropy profile. Solid black lines show one sigma systematic errors from uncertainties in background modelling. The solid green line shows the effect of subtracting the stray light emission from the core. The red points overplotted on the right are the *XMM-Newton* temperatures from Bourdin & Mazzotta (2008) found for the region away from the depression in temperature to the south east. The blue points for the temperature and entropy on the left are the for the cold depression to the south east found in Bourdin & Mazzotta (2008) and correlate well with the *Suzaku* values in the outskirts to the south east. For the density plots the solid red line is the best fit deprojected density profile found in Vikhlinin et al. (2006) using *Chandra* data. For the entropy plots the solid black line is the $r^{1.1}$ relation from Voit et al. (2005) scaled to pass through the central three points of our *Suzaku* data on the left. The same profile is shown to the right to emphasise the lower entropy in the south east.

from CMB data in Komatsu et al. 2011) near our calculated value of the virial radius.

6 EXCESS TO THE NORTH.

The projected density profile shows an excess to the North, suggesting the existence of a filament connecting Abell 2029 to Abell 2033, or contaminating emission from Abell 2033 entering the field

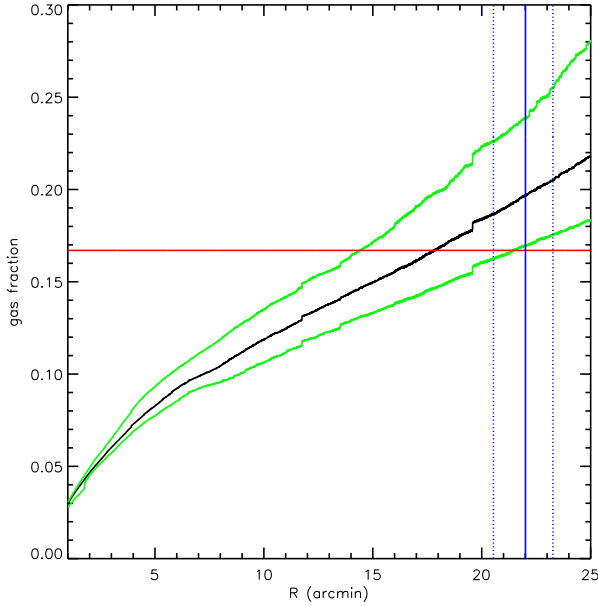


Figure 7. Gas mass fraction as a function of radius for Abell 2029. Black line shows the best fit and the green lines show the 1σ error ranges. The red horizontal line shows the cosmic mean baryon fraction as determined in Komatsu et al. (2011). The solid blue vertical line shows our measurement of r_{200} and the vertical blue dotted lines show the one sigma uncertainty in r_{200} .

of view. The existence of this structure has also been claimed in Eckert et al. (2011) who studied azimuthal variations in the surface brightness profiles of 31 galaxy clusters using archival ROSAT PSPC data, and found a significant excess connecting Abell 2029 and Abell 2033.

To check the presence of this excess we used a ROSAT PSPC pointing of the Abell 2029 and Abell 2033 system (rp800249) and examined the surface brightness profiles in the directions corresponding to the arms of the cross (using the same regions and annuli binning as used for our *Suzaku* pointings). The ROSAT PSPC data were reduced using the ROSAT Extended Source Analysis Software (ESAS, Snowden et al. 1994). We follow the same method as Eckert et al. (2011) to obtain a background subtracted, exposure corrected counts image for the R47 band (corresponding to 0.44–2.04 keV). The resulting image is shown in Fig. 8, and there is a clear bright region connecting Abell 2029 to Abell 2033.

The resulting background subtracted projected ROSAT surface brightness profile is shown in Fig. 9, where the error in the background has been added in quadrature to the error bars. We clearly see an excess to the north (red) deviating from the beta law decrease of the azimuthal average of the other directions. This is the only statistically significant deviation from azimuthal symmetry in the surface brightness profiles. We also show the corresponding vignetting corrected and background subtracted projected surface brightness profile obtained with *Suzaku* in the 0.7–2.0 keV band in Fig. 9 (where vignetting correction and background subtraction were performed following the method of Bautz et al. 2009), also showing the excess in the northern direction. The overplotted beta model is that obtained in S98 (which used different data reduction methods) as the best fit to the azimuthally averaged profile between 164 arcsecs and 1000 arcsecs.

However another possibility is that the excess is caused due to

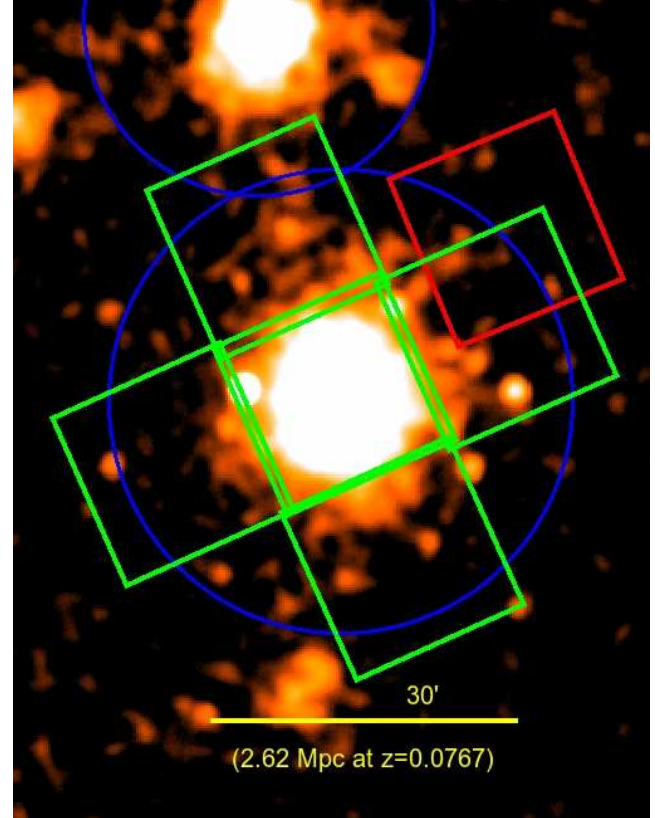


Figure 8. Exposure corrected and background subtracted ROSAT PSPC image of the Abell 2029/2033 system smoothed with a Gaussian kernel, showing indications of excess emission to the north of Abell 2029 between the two clusters. The virial radii of the two clusters are shown by the blue circles.

overlapping emission from the outskirts of Abell 2029 and Abell 2033, with no need for excess emission from a filament. Using the scaling relation, equation 4, for r_{200} we find r_{200} for Abell 2033 to be 1.5 Mpc (17.0') (using the mean temperature of 3.84 keV from ASCA found in Fukazawa et al. 2004). We found in section 5 that for Abell 2029 our *Suzaku* results imply $r_{200}=22.0^{+1.3}_{-1.4}$ arcmins. These virial radii are overplotted as the blue circles on Fig. 8, and we see that the excess emission correlates well with the region where we would expect to detect emission from the ICM of the outskirts of Abell 2033.

6.1 Spectral analysis of northern excess

The difference in redshift between Abell 2029 ($z=0.0767$) and Abell 2033 ($z=0.081$) corresponds to a distance of ~ 20 Mpc (neglecting the effect of possible peculiar velocities), meaning that if a filament exists between the two then we are seeing it along its length, increasing its surface brightness due to this preferential geometry. Such a preferential geometry has already been exploited to study a potential filament between Abell 222 and Abell 223 (Werner et al. 2008) which is viewed along its length, however as that system is located at a much higher redshift ($z=0.21$) than the Abell 2029 and Abell 2033 system its surface brightness and area of extent are both lower.

To fit for the projected properties of the northern excess, we perform a fit to the 19.5'–25.0' region to the north, and simultane-

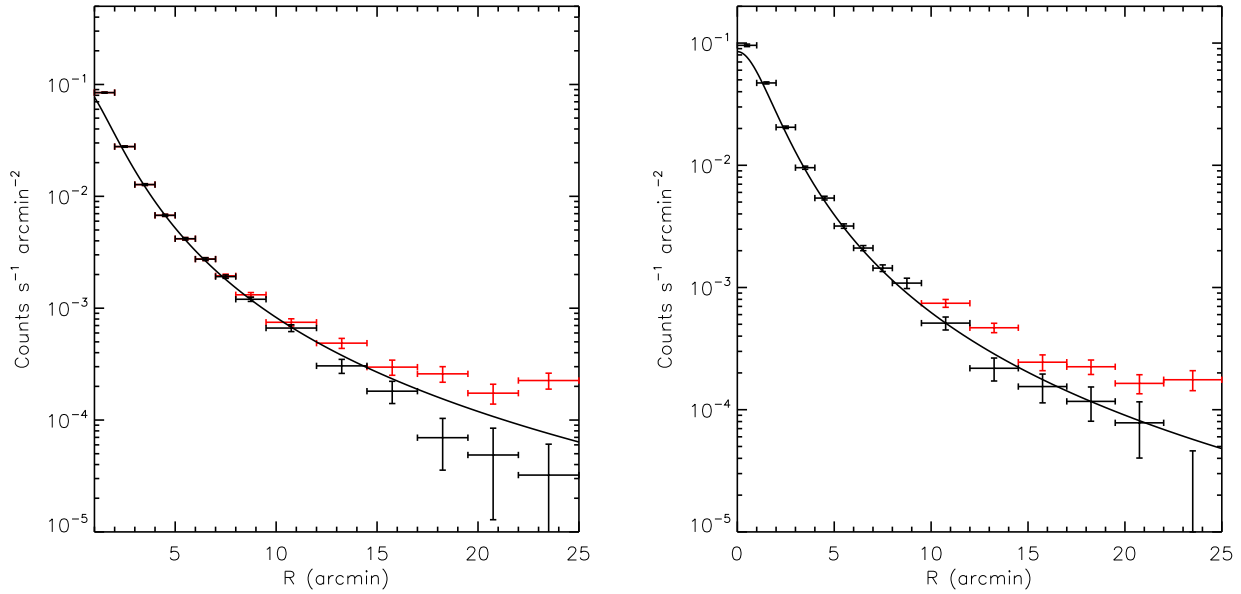


Figure 9. Left: Exposure corrected and background subtracted ROSAT PSPC surface brightness profile for the same regions analysed with *Suzaku* of the Abell 2029/2033 system in the 0.4–2.0 keV band. Right: Vignetting corrected and background subtracted *Suzaku* surface brightness profile in the 0.7–2.0 keV band, averaged over the two front illuminated detectors (XIS0 and XIS3). In both panels the black points are an azimuthal average over all directions except the north and the red points are for the northern direction only, showing a significant excess to the North with both satellites. The black solid line is the beta model found in S98 for the azimuthally averaged surface brightness profile between 164 arcsecs and 1000 arcsecs (16.7 arcmin).

ously fit the same regions in the other 4 directions which are tied to get an azimuthal average, and use this as a background model. In this way we fit the excess over the azimuthal average level to the north in the 19.5′–25.0′ region as an absorbed APEC component. The excess of the spectrum over the azimuthal average of the other directions is shown in Fig. 10. The normalisation of the excess APEC component, taking into account systematic errors in the background determination is $1.5^{+0.5}_{-0.5} \times 10^{-3} \text{ cm}^{-5}$, and the temperature is $3.6^{+1.1}_{-1.2} \text{ keV}$. This temperature appears too high for the excess to be caused by a WHIM filament connecting the two clusters (which would be expected to have a temperature around 1 keV as this gas would not have been shock heated due to accretion yet (Werner et al. 2008, Davé et al. 2001)). The temperature is more consistent with this emission originating from the outskirts of Abell 2033. Assuming that the excess emission completely originates from Abell 2033 and assuming spherical symmetry, the emission norm of the excess corresponds to a density in the range $1.0\text{--}2.0 \times 10^{-4} \text{ cm}^{-3}$ in the outskirts of Abell 2033, which seems reasonable.

Figures 4 and 9 show that the excess to the northern direction is present from a radius of 12′ outwards, but it only seems reasonable to attribute the excess at radii beyond 19.5′ as being due to overlapping emission from Abell 2033. The excess between 12′ and 19.5′ could have a number of causes. One is that the density to the north could genuinely be higher than that in other directions. Another is that we may be detecting emission from gas in a filamentary structure connecting Abell 2029 and Abell 2033.

6.2 Comparing to the spatial galaxy distribution

To investigate the nature of the excess emission between Abell 2029 and Abell 2033 further, we constructed the density field of

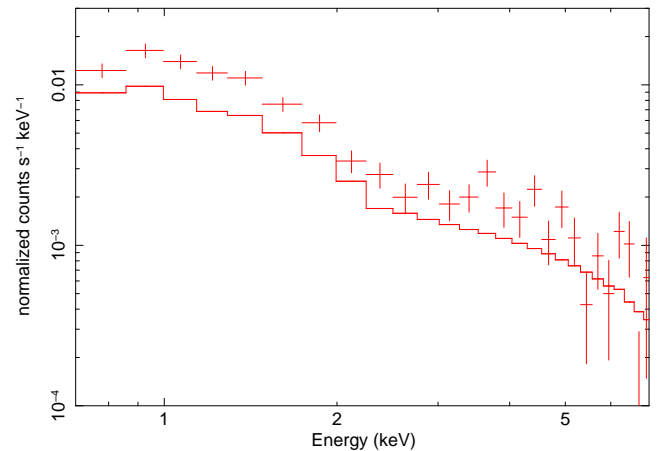


Figure 10. Spectrum of excess emission to the north. Points show spectrum of northern excess region. Line shows the azimuthal average spectrum fit for all of the other directions.

galaxies around Abell 2029 using data from the Sloan Digital Sky Survey (SDSS). Taking the photometric catalogue from SDSS Data Release 7 (Abazajian et al. 2009), we select galaxies with magnitude $i < 21.0$ and a photometric redshift within a range of $dz = 0.032$ centred on the redshift of Abell 2029, $z_c = 0.0767$. This range corresponds to the median photometric redshift uncertainty for sources of this magnitude at $z < 0.1$. The general features of the density field are not highly sensitive to the redshift range used, and the spectroscopic catalogue produces similar results though with a lower sampling density. Though the range exceeds the typical velocity dispersion of a cluster, we can easily

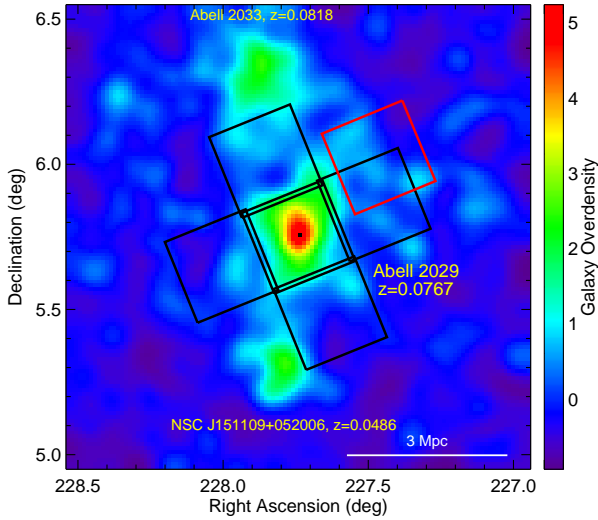


Figure 11. This shows the distribution of galaxies with magnitude $i < 21.0$ and photometric redshift $|z - z_c| < 0.016$ using SDSS data. We define the overdensity as $(\rho - \langle \rho \rangle) / \langle \rho \rangle$ where $\langle \rho \rangle$ is the mean galaxy density computed on the 16 deg^2 region centred on Abell 2029, and smooth the overdensity plot using a Gaussian kernel with a FWHM of 500 kpc at the redshift of Abell 2029.

identify peaks in the density field associated with known clusters nearby, as shown in Fig. 11. We plot the overdensity of galaxies smoothed by a Gaussian with FWHM = 500 kpc.

There is a clear excess in the galaxy density to the north which appears to originate from Abell 2033, consistent with our hypothesis that we are seeing the overlap of the virial radii of Abell 2029 and Abell 2033.

The foreground object NSC J151109+052006 is very faint in X-rays (it is visible as an extended source to the south in Fig. 8) and lies out of the field of view of the south west pointing. We simulated the expected contribution from this source in the south west pointing using XISSIM and found it to be negligible.

7 SUMMARY

We explore the ICM of the galaxy cluster Abell 2029 to higher radius than before, with no statistically significant emission detected beyond $22'$ (except for the northern pointing between Abell 2029 and Abell 2033), which is 1.9 Mpc, and is equal to our measurement of r_{200} . Excess emission is found to the north between Abell 2029 and Abell 2033 which is detected in both our *Suzaku* observations and in ROSAT PSPC observations, and the most consistent explanation for this excess emission is that it originates from Abell 2033 and we are seeing the overlap of the outskirts of the two clusters to the north.

We detect a cold feature to the SE extending out to the edge of the detected cluster ($22'$) where the ICM is significantly colder than in the other directions, consistent with the *XMM-Newton* findings of Bourdin & Mazzotta (2008) which found a temperature depression to the south east within the central $8'$. The substantial point spread function does not allow this cold feature to be traced into the central 2 annuli of the *Suzaku* pointing. The lower temperature causes the entropy profile to be lower and to flatten, indicating that the ICM in this direction is significantly out of hydrostatic equilibrium. This

may be the result of the accretion of galaxy groups along the SE direction, which has disturbed the ICM.

Away from this cold feature, the azimuthally averaged temperatures and densities are consistent with previous findings, with the entropy profile rising in the outskirts but not as steeply as the $r^{1.1}$ powerlaw predicted due to pure gravitational hierarchical structure formation, a result which has also been found for other clusters [Abell 1795, (Bautz et al. 2009), the Perseus cluster (Simionescu et al. 2011), and Abell 2142 (Akamatsu et al. 2011)].

ACKNOWLEDGEMENTS

SAW is supported by STFC, and ACF thanks the Royal Society. MRG acknowledges support from an NSF Graduate Research Fellowship and NASA grant NNX10AR49G. This research has used data from the *Suzaku* telescope, a joint mission between JAXA and NASA. We acknowledge the use of data made available through the SDSS archive. Funding for the Sloan Digital Sky Survey (SDSS) has been provided by the Alfred P. Sloan Foundation, the Participating Institutions, the National Science Foundation, the U.S. Department of Energy, the Japanese Monbukagakusho, and the Max Planck Society. This research has made use of the NASA/IPAC Extragalactic Database (NED) which is operated by the Jet Propulsion Laboratory, California Institute of Technology, under contract with the National Aeronautics and Space Administration.

REFERENCES

- Abazajian K. N., Adelman-McCarthy J. K., Agüeros M. A., Allam S. S., Allende Prieto C., An D., Anderson K. S. J., Anderson S. F., Annis J., Bahcall N. A., et al. 2009, *ApJS*, 182, 543
- Akamatsu H., Hoshino A., Ishisaki Y., Ohashi T., Sato K., Takei Y., Ota N., 2011, *PASJ*, 63, 1019
- Allen S. W., Rapetti D. A., Schmidt R. W., Ebeling H., Morris R. G., Fabian A. C., 2008, *MNRAS*, 383, 879
- Arnaud M., Pointecouteau E., Pratt G. W., 2005, *A&A*, 441, 893
- Bautz M. W., Miller E. D., Sanders J. S., Arnaud K. A., Mushotzky R. F., Porter F. S., Hayashida K., Henry J. P., Hughes J. P., Kawaharada M., Makashima K., Sato M., Tamura T., 2009, *PASJ*, 61, 1117
- Bourdin H., Mazzotta P., 2008, *A&A*, 479, 307
- Burns J. O., Skillman S. W., O'Shea B. W., 2010, *ApJ*, 721, 1105
- Clarke T. E., Blanton E. L., Sarazin C. L., 2004, *ApJ*, 616, 178
- Davé R., Cen R., Ostriker J. P., Bryan G. L., Hernquist L., Katz N., Weinberg D. H., Norman M. L., O'Shea B., 2001, *ApJ*, 552, 473
- De Luca A., Molendi S., 2004, *A&A*, 419, 837
- Eckert D., Molendi S., Gastaldello F., Rossetti M., 2011, *A&A*, 529, A133+
- Eckert D., Vazza F., Ettori S., Molendi S., Nagai D., Lau E. T., Roncarelli M., Rossetti M., Snowden S. L., Gastaldello F., 2011, *ArXiv e-prints*
- Einasto M., Einasto J., Tago E., Müller V., Andernach H., 2001, *AJ*, 122, 2222
- Fukazawa Y., Makishima K., Ohashi T., 2004, *PASJ*, 56, 965
- Gastaldello F., Ettori S., Balestra I., Brighenti F., Buote D. A., de Grandi S., Ghizzardi S., Gitti M., Tozzi P., 2010, *A&A*, 522, A34+

George M. R., Fabian A. C., Sanders J. S., Young A. J., Russell H. R., 2009, *MNRAS*, 395, 657

Hoshino A., Patrick Henry J., Sato K., Akamatsu H., Yokota W., Sasaki S., Ishisaki Y., Ohashi T., Bautz M., Fukazawa Y., Kawano N., Furuzawa A., Hayashida K., Tawa N., Hughes J. P., Kokubun M., Tamura T., 2010, *PASJ*, 62, 371

Humphrey P. J., Buote D. A., Brighenti F., Flohic H. M. L. G., Gastaldello F., Mathews W. G., 2011, *ArXiv e-prints*

Ishisaki Y., Maeda Y., Fujimoto R., Ozaki M., Ebisawa K., Takahashi T., Ueda Y., Ogasaka Y., Ptak A., Mukai K., Hamaguchi K., 2007, *PASJ*, 59, 113

Kalberla P. M. W., Burton W. B., Hartmann D., Arnal E. M., Bajaja E., Morras R., Pöppel W. G. L., 2005, *A&A*, 440, 775

Kawaharada M., Okabe N., Umetsu K., Takizawa M., Matsushita K., Fukazawa Y., Hamana T., Miyazaki S., Nakazawa K., Ohashi T., 2010, *ApJ*, 714, 423

Komatsu E., Smith K. M., Dunkley J., Bennett C. L., Gold B., Hinshaw G., Jarosik N., Larson D., Nolte M. R., 2011, *ApJS*, 192, 18

Kushino A., Ishisaki Y., Morita U., Yamasaki N. Y., Ishida M., Ohashi T., Ueda Y., 2002, *PASJ*, 54, 327

Lewis A. D., Stocke J. T., Buote D. A., 2002, *ApJ*, 573, L13

Miyoshi S., Tanaka N., Yoshimura M., Yamashita K., Furuzawa A., Futamura T., Hudaverdi M., 2005, *Advances in Space Research*, 36, 752

Molendi S., De Grandi S., 1999, *A&A*, 351, L41

Moretti A., Campana S., Lazzati D., Tagliaferri G., 2003, *ApJ*, 588, 696

Moretti A., Gastaldello F., Etori S., Molendi S., 2011, *A&A*, 528, A102+

Moretti A., Pagani C., Cusumano G., Campana S., Perri M., Abbey A., Ajello M., Beardmore A. P., Burrows D., Chincarini G., Godet O., Guidorzi C., Hill J. E., Kennea J., Nousek J., Osborne J. P., Tagliaferri G., 2009, *A&A*, 493, 501

Reiprich T. H., Hudson D. S., Zhang Y., Sato K., Ishisaki Y., Hoshino A., Ohashi T., Ota N., Fujita Y., 2009, *A&A*, 501, 899

Sarazin C. L., Wise M. W., Markevitch M. L., 1998, *ApJ*, 498, 606

Serlemitsos P. J., Soong Y., Chan K.-W., Okajima T., Lehan J. P., Maeda Y., Itoh K., 2007, *PASJ*, 59, 9

Simionescu A., Allen S., Mantz A., Werner N., 2011, in J.-U. Ness & M. Ehle ed., *The X-ray Universe 2011 Baryons at the edge of the X-ray brightest galaxy cluster*. p. 152

Simionescu A., Allen S. W., Mantz A., Werner N., Takei Y., Morris R. G., Fabian A. C., Sanders J. S., Nulsen P. E. J., George M. R., Taylor G. B., 2011, *Science*, 331, 1576

Snowden S. L., Collier M. R., Kuntz K. D., 2004, *ApJ*, 610, 1182

Snowden S. L., McCammon D., Burrows D. N., Mendenhall J. A., 1994, *ApJ*, 424, 714

Snowden S. L., Mushotzky R. F., Kuntz K. D., Davis D. S., 2008, *A&A*, 478, 615

Tawa N., Hayashida K., Nagai M., Nakamoto H., Tsunemi H., Yamaguchi H., Ishisaki Y., Miller E. D., Mizuno T., Dotani T., Ozaki M., Katayama H., 2008, *PASJ*, 60, 11

Uson J. M., Boughn S. P., Kuhn J. R., 1991, *ApJ*, 369, 46

Vikhlinin A., Kravtsov A., Forman W., Jones C., Markevitch M., Murray S. S., Van Speybroeck L., 2006, *ApJ*, 640, 691

Vikhlinin A., Kravtsov A. V., Burenin R. A., Ebeling H., Forman W. R., Hornstrup A., Jones C., Murray S. S., Nagai D., Quintana H., Voevodkin A., 2009, *ApJ*, 692, 1060

Vikhlinin A., Markevitch M., Murray S. S., Jones C., Forman W., Van Speybroeck L., 2005, *ApJ*, 628, 655

Voit G. M., Kay S. T., Bryan G. L., 2005, *MNRAS*, 364, 909

Werner N., Finoguenov A., Kaastra J. S., Simionescu A., Dietrich J. P., Vink J., Böhringer H., 2008, *A&A*, 482, L29

APPENDIX A: FITTING FOR THE GALACTIC X-RAY BACKGROUND

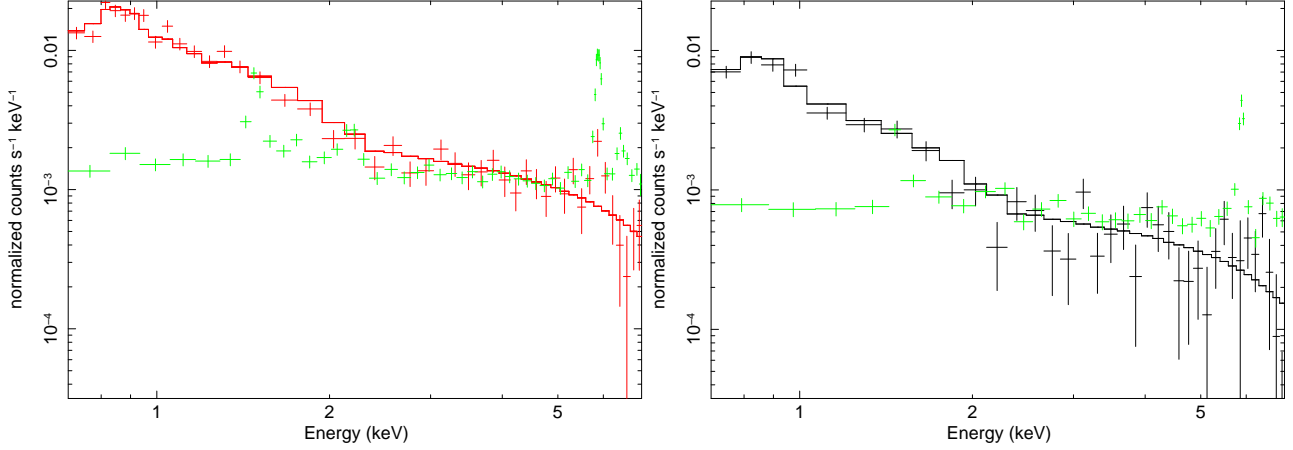


Figure A1. Fitting to the *Suzaku* background regions in the NW offset pointing. Left shows the fit to the 25'-29' annulus, and right shows the fit to the 29' to 34' annulus using. Overplotted in green in the NXB level. Note that the areas of extraction for the two spectra are different, thus explaining the different normalised count rates on the y axis.

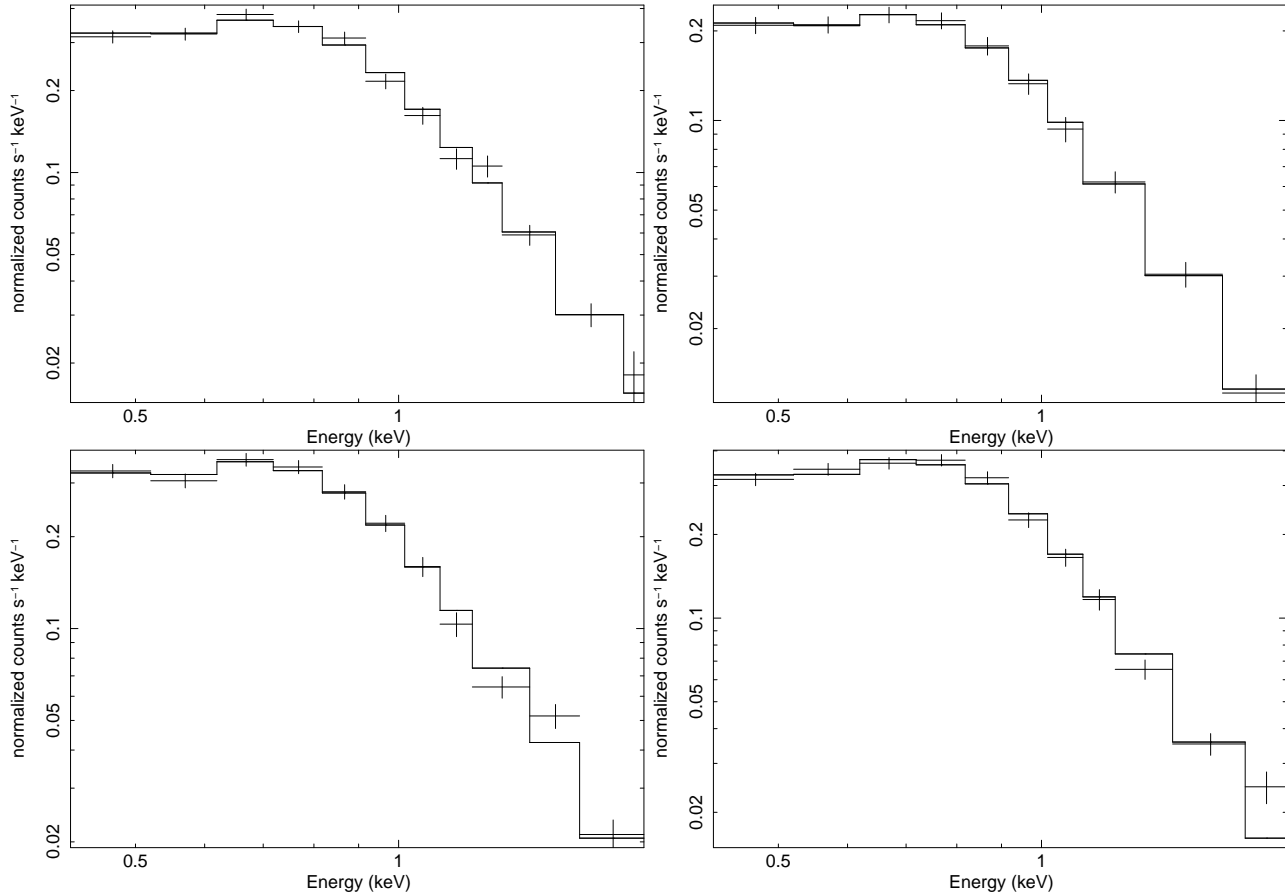


Figure A2. Fitting to ROSAT PSPC background regions in an annulus between 30' and 50' using the same model found using the *Suzaku* background pointings. Top left is for the NW, top right is for the NE, bottom left is for the SE and bottom right is for the SW. These fits give the ranges in the normalisations of the background parameters shown in table 3 which are used to understand the expected spatial variation of the soft X-ray background. Note that the areas of extraction for the four spectra are different, thus explaining the different normalised count rates on the y axis.

APPENDIX B: SPECTRAL FITTING

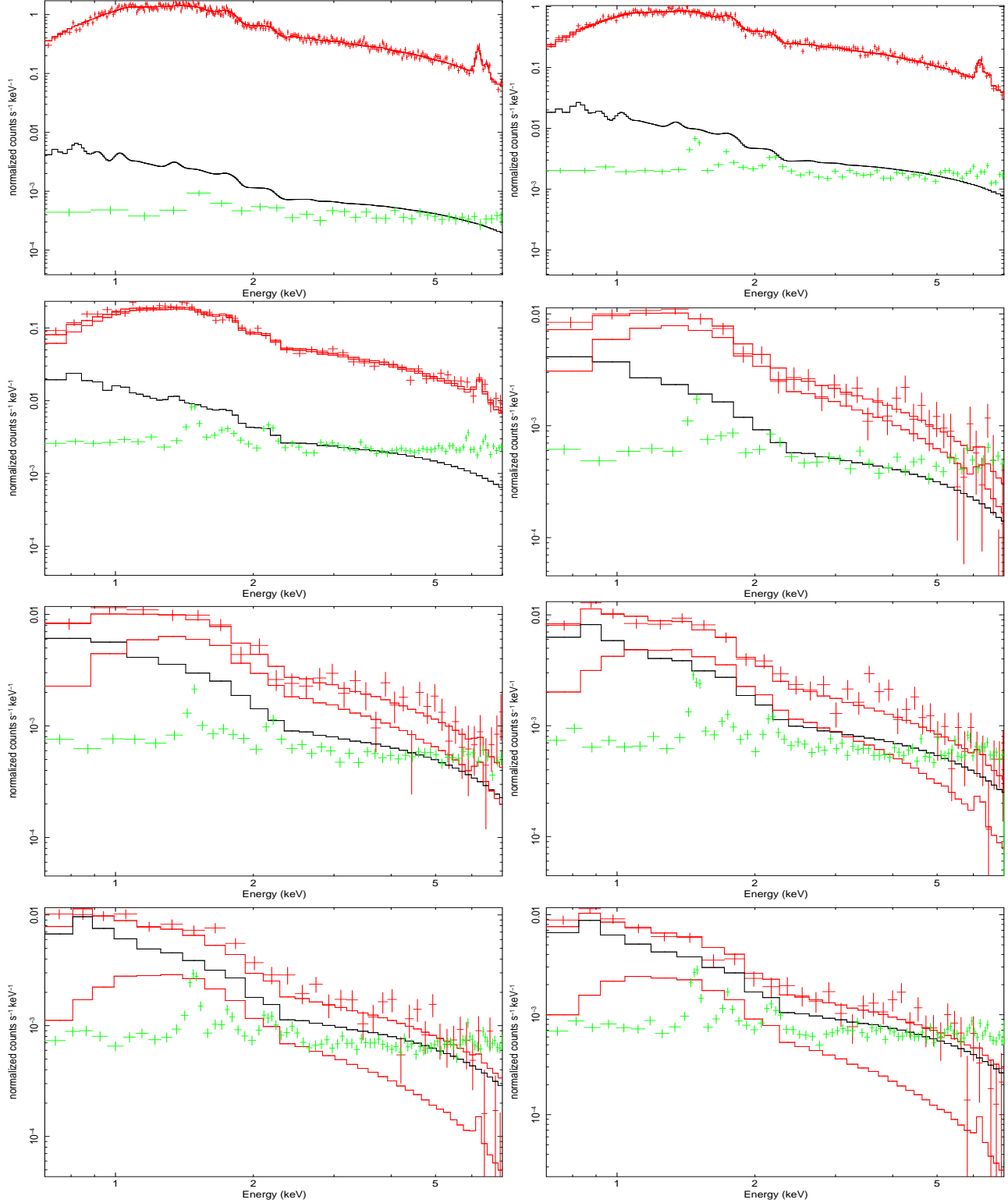


Figure B1. Spectral fitting to the XIS0 and XIS3 data simultaneously. The spectra are for the azimuthally averaged fit (excluding the north and the south east) used to obtain the results in the left column of Fig. 6, but here we show the projected fits for simplicity. In reading order the spectra correspond to increasing radii annuli, which are between $0.0'-2.5'$, $2.5'-6.0'$, $6.0'-9.5'$, $9.5'-12.0'$, $12.0'-14.5'$, $14.5'-17.0'$, $17.0'-19.5'$ and $19.5'-22.0'$. The central 3 annuli are integrated across all azimuth and are from the central pointing only. The red lines through the points represent the best fits (background plus cluster emission), while the lower red line shows the excess over the background level (shown as the black solid line) modelled in these projected fits as an absorbed APEC component. The NXB level is overplotted in green.